Formation of lower bainite in a high carbon steel – an in-situ synchrotron XRD study

DOI:
10.1016/j.jmrt.2022.05.025

Document Version
Final published version

Available online at www.sciencedirect.com

jmr&t Journal of Materials Research and Technology

journal homepage: www.elsevier.com/locate/jmrt

Original Article

Formation of lower bainite in a high carbon steel – an in-situ synchrotron XRD study

D. Foster [a,*], M. Paladugu [b,**], J. Hughes [a], M. Kapousidou [a], U. Islam [a], A. Stark [c], N. Schell [c], E. Jimenez-Melero [a]

[a] Materials Performance Centre, Department of Materials, The University of Manchester, M13 9PL, UK
[b] The Timken Company World Headquarters (WHQ), North Canton, OH, 44720, USA
[c] Helmholtz-Zentrum Hereon, Max-Planck-Straße 1, 21502 Geesthacht, Germany

ARTICLE INFO

Article history:
Received 16 February 2022
Accepted 2 May 2022
Available online 9 May 2022

Keywords:
SAE 52100 steel
Austempering
Bainite reaction
Lattice distortion
Synchrotron X-ray diffraction
Dilatometry

ABSTRACT

The microstructural evolution of and simultaneous dimensional changes in high-carbon SAE 52100 bearing steel were monitored continuously during austempering for 120 min at selected temperatures in the range of 210 °C-270 °C, and also during its subsequent tempering to 340 °C for an additional 120 min, via high-energy X-ray diffraction in real time and in-situ dilatometry. The austenite-to-bainitic ferrite transformation induces lattice defects and internal lattice stresses that increase with austempering time and at lower austempering temperatures. These changes are evidenced by the increase in the full-width half-maximum of the relevant reflections in X-ray diffraction. The lattice parameter of bainitic ferrite takes its highest value during the early stages of austempering, and then gradually decreases as the transformation progresses. This observation points to an initial state of carbon supersaturation in the ferritic lattice that is likely reducing due to carbon segregation close to dislocations, fine carbide precipitation within the bainitic ferrite, and carbon partitioning into the surrounding austenite. The carbon partitioning into austenite is evidenced in particular at the higher austempering temperatures of 240 °C and 270 °C, at which there is a noticeable increase in the lattice parameter of the remaining austenite at longer times. The dimensions of the bearing steel specimens are governed by the volume change due to the formation of bainitic ferrite during austempering and by the relaxation of its lattice distortion during tempering at 340 °C in the absence of further phase transformation.

1. Introduction

Roller bearings are engineering components designed to transfer force, torque and speed with minimal friction drag through a mechanical system to perform work [1]. During bearing operation, complex sub-surface stress states are generated as a consequence of Hertzian contact stresses of several magnitudes of GPa, together with cyclic shear stresses, potentially leading to the life-limiting phenomenon of rolling

* Corresponding author.
** Corresponding author.
E-mail addresses: daniel.foster-7@postgrad.manchester.ac.uk (D. Foster), mohan.paladugu@timken.com (M. Paladugu).
https://doi.org/10.1016/j.jmrt.2022.05.025

contact fatigue (RCF) [1–3]. The fatigue and stress state generated from RCF can cause surface and subsurface damage and lead to cracking and spalling of the bearing during service. Material selection and bearing design are therefore governed by the material's resistance to RCF and surface wear degradation [3,4], together with the potential chemical attack and hydrogen embrittlement in aggressive service environments [5,6].

Roller bearings are predominantly manufactured using through-hardened high-carbon (>0.8 wt.%C) SAE 52100 steel containing <5 wt.% total alloying elements [1–3]. This steel grade offers easiness of machining in the as-spheroidised condition and high hardenability. Once machined into the bearing component, the steel is heated to the austenitisation temperature (≥840 °C), followed by oil quenching to 50 °C to form a martensitic structure. The steel is finally tempered between 160 °C and 180 °C, presenting hardness at values of 61–65 HRC and an ultimate tensile strength of >2 GPa. This standard quench and tempering (QT) process yields a final microstructure of tempered martensite, retained austenite (<15 vol.%) and spherical Fe_3C particles (~2–3 vol.%) [3,7,8].

The subsurface evolution of lattice defects and microplasticity in SAE 52100 bearings is monitored by depth-profiling residual stress distributions and also by local changes in the full-width half-maximum (FWHM) of martensitic (α') reflections in X-ray diffraction with respect to the FWHM of the core structure [9–13]. In fact, the FWHM of the $\{200\}_{\alpha'}$ is reported to present a linear relationship with the material's hardness [14], and the endurable Hertzian pressure depends on the material's hardness after heat treatment [15].

Alternatively, bainitic austempering (B) offers the possibility of widening the palette of material properties and bearing performance offered by the established QT process [16–18] without having to resort to enhanced levels of alloying elements as with SAE 52100 steel [19,20]. This austempering process involves salt bath quenching the steel after austenitisation to temperatures in the range of ~200 °C–350 °C, notably above but relatively close to the martensite start temperature of the steel, and isothermally holding the steel to form lower bainite before the final cooling to room temperature [3,21,22].

An increase in austempering temperature from 250 °C to 290 °C is reported to reduce the hardness of bainitic ferrite from 60 HRC to 38–39 HRC [23,24]. Fragmented experimental data from literature suggests enhanced levels of toughness in lower bainitic structures and potentially higher resistance to hydrogen uptake from the environment compared to tempered martensite at an equivalent hardness level [17,19,25]. Additionally, the austempering step also minimises the occurrence of quench distortion and cracks and eliminates the need of a further tempering step during bearing manufacture [25,26].

Capitalising on the full potential of bainitic austempering in high-carbon bearing steels demands a reliable and mechanistic understanding of the microstructural evolution in high-carbon bearing steel as a function of austempering parameters, along with a thorough grasp of how those thermally induced microstructural changes affect the dimensions and hardness of the material. In this work, we aimed to monitor in real time the evolution of the constituent phases and lattice distortions in the austempering regime of 210 °C–270 °C, and thereafter the microstructural changes during tempering at 340 °C, by performing in-situ dilatometry with a high-energy synchrotron diffraction beamline. During this process, the changes in volume fractions, lattice parameters and FWHM of the X-ray diffraction peaks of the phases that developed were probed, and such changes are discussed with respect to length changes in the dilatometer sample. The resultant microstructure for selected process parameters also provides a reference state when assessing the service performance of those austempered steels [12,27].

2. Experimental details

SAE 52100 steel was received in the as-spheroidised condition. Its chemical composition is given in Table 1. Dilatometry samples with a diameter of 4 mm and a length of 10 mm were machined from the stock material and inserted sequentially into a modified Bähr DIL 805 A/D dilatometer [28,29], mounted on the P07 High Energy Materials Science Beamline [30] in PETRA III at the DESY synchrotron facility in Hamburg, Germany. An in-situ synchrotron X-ray diffraction (SXRD) experiment was performed in transmission geometry during full austenitisation and austempering cycles at four selected austempering temperatures. A monochromatic beam of energy $E = 87.1$ keV ($\lambda = 0.14235$ Å) and size of 0.5×0.5 mm^2 illuminated the cylindrical sample (see Fig. 1a).

The sample was induction heated from room temperature to 860 °C at a rate of 3 °C/s and held at that temperature for 20 min for austenitisation, before being helium gas quenched at a rate of 60 °C/s to either 210 °C, 220 °C, 240 °C or 270 °C. The samples are labeled accordingly as "B210C," "B220C," "B240C" or "B270C". They were then held at the selected austempering temperature for 120 min and finally air cooled to room temperature. The sample temperature was measured continuously via a thermocouple spot welded to the sample. An additional sample was chosen to undergo a similar full thermal cycle at an austempering temperature of 240 °C for 120 min, but the heat treatment included an additional subsequent tempering step at 340 °C for 120 min before the final cooling to room temperature.

Two-dimensional diffraction patterns were collected with a PerkinElmer XRD 1621 flat panel detector at a distance of 1405 mm behind the sample at a rate of 1 Hz, which was increased to 10 Hz during sample quenching. LaB_6 was used as the calibrant (Standard NIST Reference Material 660c). The recorded 2D dataset was integrated using the DAWN software package [31], and the resultant 1D patterns as a function of temperature and time for each sample were subsequently analysed using the Rietveld method [32] implemented in the FullProf Suite software package [33]. The Rietveld analysis included the refinement of the scale factor, volume fraction,

Table 1 – Chemical composition (wt.%) of the SAE 52100 steel used in this study.

C	Cr	Mn	Si	Cu	Ni	Al	Fe
1.005	1.46	0.32	0.27	0.19	0.1	0.024	Bal.

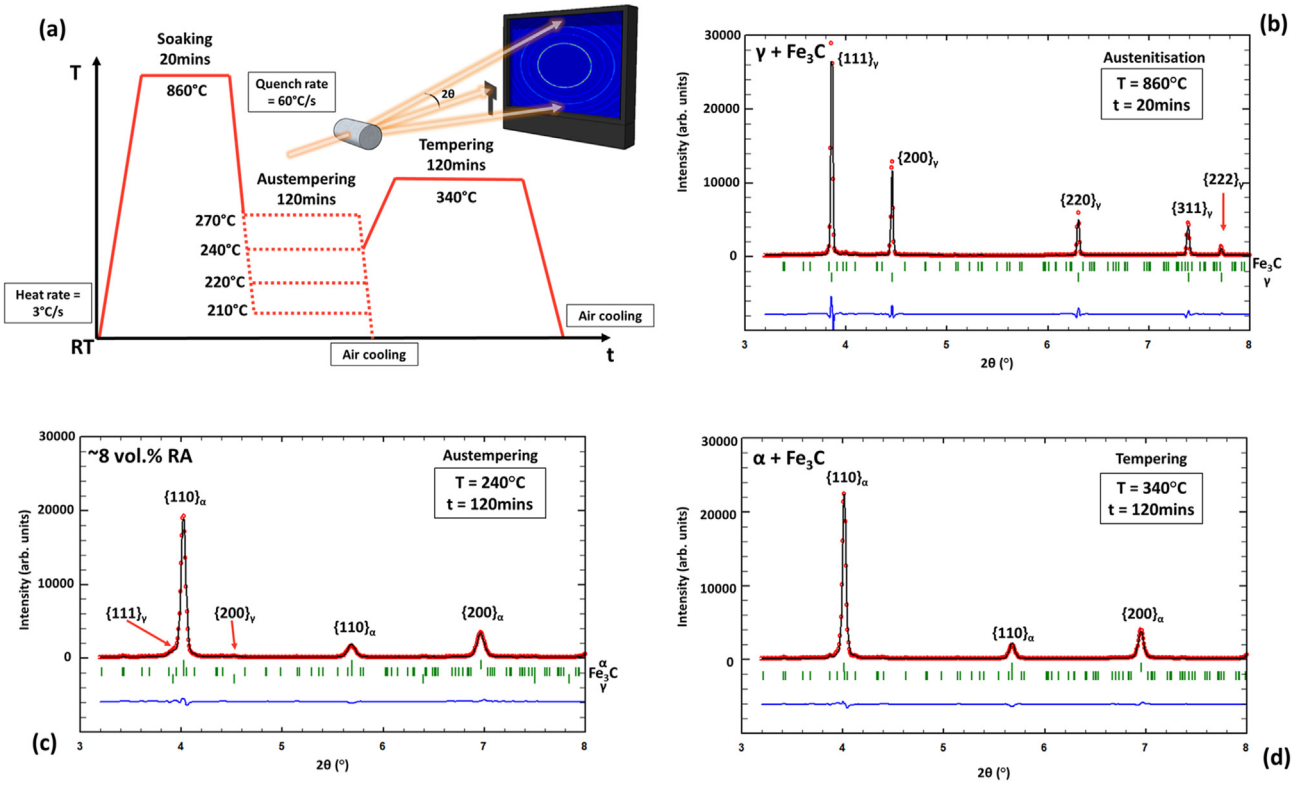

Fig. 1 – (a) Schematic of the time–temperature diagram for the selected austempering regimes performed in-situ during the synchrotron experiment. All instances of heating were at a rate of 3 °C/s, and quenching was at 60 °C/s. A schematic representation is also shown of the high-energy synchrotron X-ray diffraction setup in transmission geometry performed in combination with dilatometry. An X-ray beam with a size 0.5 × 0.5 mm² and an energy of 87.1 keV ($\lambda = 0.14235$ Å) illuminated the center of the cylindrical dilatometry sample. (b) The Rietveld analysis of a 1D diffraction pattern after 20 min soaking at 860 °C. (c) and (d) The Rietveld analysis of the final 1D diffraction pattern acquired at 120 min of austempering at 240 °C and the final 1D diffraction pattern acquired at 120 min of tempering at 340 °C, after the sample was austempered for 120 min at 240 °C. The green rows of vertical lines correspond to orthorhombic cementite (Fe_3C), face-centered cubic austenite (γ), and body-centered cubic bainitic ferrite (α) and are labelled to the right of each plot.

lattice parameter and full-width half-maximum (FWHM) corresponding to the phases present in the microstructure at each temperature–time combination. Volume fractions were calculated from the relative intensities during Rietveld refinement [32,33] that included three individual crystallographic phases: BCC bainitic ferrite, FCC austenite, and orthorhombic Fe_3C. Accurate determination of phase parameters was only possible for volume fractions above ~2 vol.%. No significant texture effects were detected. Bainitic ferrite is considered the BCC component of the bainite constituent generated from austenite during austempering. Any reference hereunder to the lattice parameter, volume fraction or FWHM of the bcc phase, or the use of the subscript 'α', is reflective of 'bainitic ferrite'. The $\{110\}/\{011\}_{\alpha'}$ and $\{002\}/\{200\}_{\alpha'}$ doublets, characteristic of tetragonal symmetry as in martensitic steels, were not detected in the diffraction patterns during austempering within experimental resolution. Therefore, the bainitic ferrite was analysed based on the cubic symmetry of its unit cell.

Complementarily to the in-situ synchrotron XRD measurements, Vickers hardness was also measured using a 0.5 kg load at representative microstructural states during the thermal cycle, together with an assessment of the microstructural morphology using an FEI Versa scanning electron microscope (SEM). The metallographic samples for SEM characterisation were etched using a 2 vol.% nital solution.

3. Results

3.1. *Bainite formation during austempering*

The as-spheroidised samples were initially austenitised at 860 °C for 20 min. After this period, the microstructure was comprised of ~3 vol.% Fe_3C embedded in an austenitic matrix (see Fig. 1b). The mass balance in the austenite-cementite region yielded a carbon content in austenite of $x_C^{\gamma} \sim 0.830$ *wt.*% after 20 min, whereas the average austenite grain size was ~15 μm with a standard deviation of 1.7 μm (see Fig. S1) [27]. Afterwards, the samples were helium gas quenched, each to a target austempering temperature of either 210 °C, 220 °C, 240 °C or 270 °C, as exemplified in Fig. 1a. The time dependence of the volume fraction of the bainitic ferrite is shown in Fig. 2a for each austempering temperature,

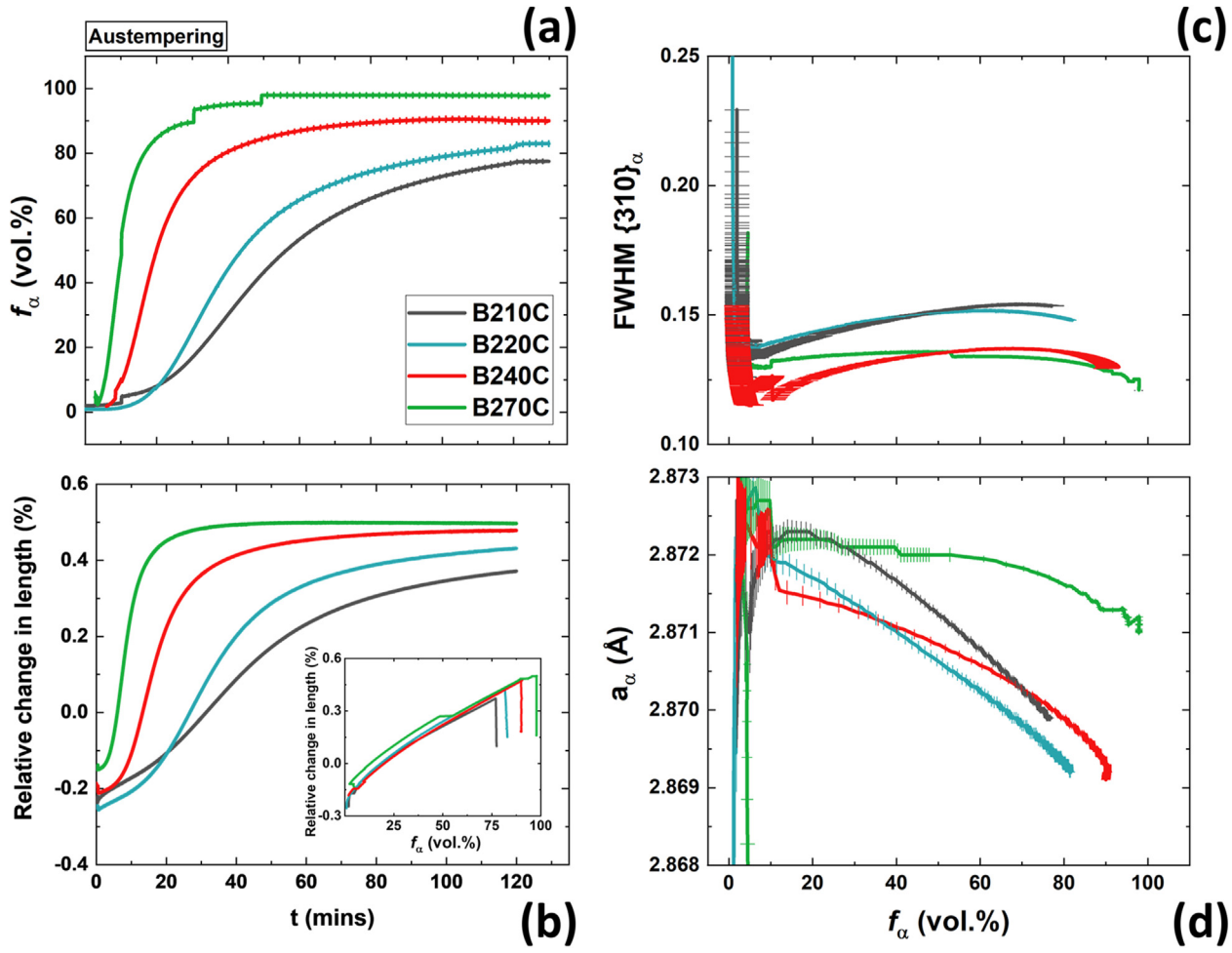

Fig. 2 – (a) Volume fraction of bainitic ferrite as a function of austempering time for selected austempering temperatures, up to the maximum of ~97 vol.%, with the remainder (~3 vol.%) occupied by cementite; (b) the corresponding relative change in sample length, calculated from the change in sample length with respect to the initial condition for each sample, as measured directly and continuously via dilatometry. (c) The FWHM of the $\{310\}_\alpha$ reflection and (d) the corresponding bainite lattice parameter, a_α, as a function of the volume fraction of bainite formed.

where t = 0 min marks the collection of the first diffraction pattern upon reaching the target temperature.

In all samples, an incubation period for the bainite transformation that produced at least 5 vol.% bainite was observed. This incubation period lasted for ~9 min at 240 °C and ~5 min at 270 °C (see Table 2). The rate of austenite transformation increased with temperature. Fig. 1c shows an illustrative example of the 1D diffraction pattern after 120 min at the austempering temperature of 240 °C. The sample austempered at 270 °C was the only sample to complete the bainite reaction within the 120 min of austempering time of this experiment, with austenite transforming completely to bainitic ferrite in ~50 min. The final phase fractions of bainitic ferrite for the B210C, B220C, and B240C samples were 77.5 ± 0.7, 83.0 ± 0.8, and 90.0 ± 1.1 vol.%, respectively.

The symmetry of the bainitic ferrite is evidenced in the raw XRD data presented in Fig. 3a. This diffraction pattern was taken at 11.3 min into the austempering regime at 210 °C, following the incubation period. The sample presented a volume fraction of bainitic ferrite of 5.0 ± 0.5 vol. % at this instance. Subsequent patterns at f_α ~10 vol.% and ~20 vol.% are shown in Fig. 3b and c and , respectively, as the austenite-to-bainitic ferrite transformation progressed. The $\{002\}/\{200\}_{\alpha'}$ doublet characteristic of tetragonal symmetry of martensite ($f_{\alpha'}$ ~80 vol.%) is shown for comparison in Fig. 3d for a SAE 52100 steel quenched to 50 °C and for an experimental resolution equivalent to the current study [34]. Furthermore, no significant changes in cementite fraction with time were detected in the XRD patterns during austempering. Its volume fraction was measured at ~2–3 vol.% Fe_3C for all austempering temperatures studied in this work. Evidence of transition carbides were not detected in the recorded XRD patterns of this study.

The microstructural morphology of the steel as a function of austempering temperatures of 220, 240, 270 and 300 °C after a period of 120 min is shown in Fig. 4, together with the measured Vickers hardness ($HV_{0.5}$) at each temperature. The SEM images in Fig. 4 show long carbide morphologies throughout the whole micrographs, along with a small number spherical Fe_3C particles [35]. The inclusion of an extra

Table 2 – Lattice parameter (a_γ) and FWHM of the {311} reflection of austenite (γ) at the start of austempering (t = 0 min) for each austempering temperature (T_{aus}) probed in this study. The volume fraction of bainitic ferrite (f_α), together with the lattice parameter and FWHM of bainitic ferrite (α) and austenite (γ), measured at the end of austempering (t = 120 min), are also listed.

T_{aus} (°C)	a_γ (t = 0 min) (Å)	FWHM $\{311\}_\gamma$ (t = 0 min)	f_α (t = 120 min) (vol.%)	a_α (t = 120 min) (Å)	FWHM $\{310\}_\alpha$ (t = 0 min)	a_γ (t = 120 min) (Å)	FWHM $\{311\}_\gamma$ (t = 120 min)	Incubation Period (min)
210	3.60590(2)	0.0290	77.0(6)	2.86990(4)	0.1536	3.60070(8)	0.0620	11.304
220	3.60680(3)	0.0290	81.7(10)	2.86260(7)	0.1480	3.60130(3)	0.0789	17.294
240	3.60820(3)	0.0290	89.9(10)	2.86910(4)	0.1293	3.60690(7)	0.1399	8.521
270	3.61120(3)	0.0290	97.9(8)	2.87100(3)	0.1211	–	–	4.528

austempering temperature of 300 °C beyond the samples measured in the in-situ portion of this work was chosen to highlight the progressive changes in carbide aspect ratio and in Vickers hardness. The spherical carbide particles are considered remnants from the initial spheroidised state of the steel (Fig. S1), which did not dissolve completely during austenitisation at 860 °C. In addition, the long carbides become somewhat coarser with increasing austempering temperature. At the lower temperatures, it is also possible to detect the presence of small retained austenite (RA) islands within the carbide morphologies (shown in Fig. 4a). These microstructural morphologies were accompanied by a reduction in hardness from 760 (210 °C) to 610 $HV_{0.5}$ (300 °C).

As the transformation progressed, a continuous increase in sample length was observed in all samples. This change in length closely followed the transformation rate (see Fig. 2b). The relative change in sample length measured after air cooling to room temperature after 120 min of austempering increased with the austempering temperature from 210 °C to 240 °C, but the change in length was observed to decrease when the austempering temperature was increased to 270 °C (see Fig. 5c).

The FWHM of the $\{310\}_\alpha$ reflection and lattice parameter of bainitic ferrite (a_α) were measured continuously during austempering and are plotted as a function of the phase fraction of the forming bainitic ferrite in Fig. 2c and d and . During the initial stages of bainite formation, the FWHM of the $\{310\}_\alpha$ reflection reached a maximum for each sample, but dropped significantly before ~10 vol.% of bainitic ferrite was formed. During further transformation, each sample experienced a steady increase in FWHM until ~50 vol.% bainitic ferrite was formed in the B240C and B270C samples, ~60 vol.% in the B220C, and ~70 vol.% in the B210C. The FWHM thereafter proceeded to decrease for the remainder of the austempering.

Fig. 5a shows the final FWHM value (red triangles) at ~20 °C after the samples were allowed to air cool to room temperature. The FWHM value reduced with increasing austempering temperature. Furthermore, all samples showed relatively high values of lattice parameter in the bainitic ferrite at the start of austempering, with gradual reduction as the transformation progressed (see Fig. 2d). The relative change in lattice parameter decreased at higher austempering temperatures, and at 270 °C, the change in lattice parameter became subtle. However, the room temperature lattice parameter of the B270C sample was somewhat higher than for the B240C sample. Fig. 6a shows the overall reduction in the lattice parameter of the bainitic ferrite measured at room temperature for higher austempering temperatures.

3.2. Austenite evolution during austempering

Fig. 7 displays the amount of austenite transformed into bainitic ferrite as a function of temperature and time, together with the variation in austenite lattice parameter (a_γ) and in FWHM of the $\{311\}_\gamma$ reflection with volume fraction of untransformed austenite. The evolution of these parameters and the equivalent for bainitic ferrite with respect to austempering time is available for reference in Fig. S2. For all samples, the lattice parameter decreased gradually as more austenite transformed into bainitic ferrite. The relative change in lattice parameter was similar in the B210C and B220C samples, whereas the rate of change was lower in B240C and especially in the B270C sample (see Fig. 6b).

In the latter two samples, an increase was detected in the austenite lattice parameter with decreasing volume fraction when approx. 12–15 vol.% austenite remained untransformed. The FWHM behavior of the $\{311\}_\gamma$ reflection was relatively similar across all samples, in which a gradual linear increase was seen until ~50 vol.% of austenite had transformed into bainitic ferrite. After this point, an exponential increase in FWHM magnitude was observed until the final volume fraction of austenite was reached at each austempering temperature. Fig. 5b shows the austenite lattice parameter (blue squares) and FWHM of the $\{311\}_\gamma$ reflection (red triangles) as measured at room temperature post-austempering (see also Table 3). Both the austenite lattice parameter and FWHM are directly proportional to the austempering temperature.

3.3. Tempering after austempering at 240 °C

In order to assess the tempering behavior of the austempered microstructure containing untransformed austenite, an additional sample was tempered at 340 °C for 120 min after having undergone an isothermal austempering step at 240 °C for 120 min (see Fig. 8). During the heating step from 240 to 340 °C, ~1 vol.% of the austenite retained at the end of austempering transformed into ferrite. This phase transformation induced a significant increase in both the austenite lattice parameter and in the FWHM of the $\{311\}_\gamma$ reflection. Upon reaching 340 °C, ~2.5 vol.% of austenite remained untransformed in the microstructure, which further reduced to ~2 vol.% within <1 min of tempering (see Fig. 8a). It was at this

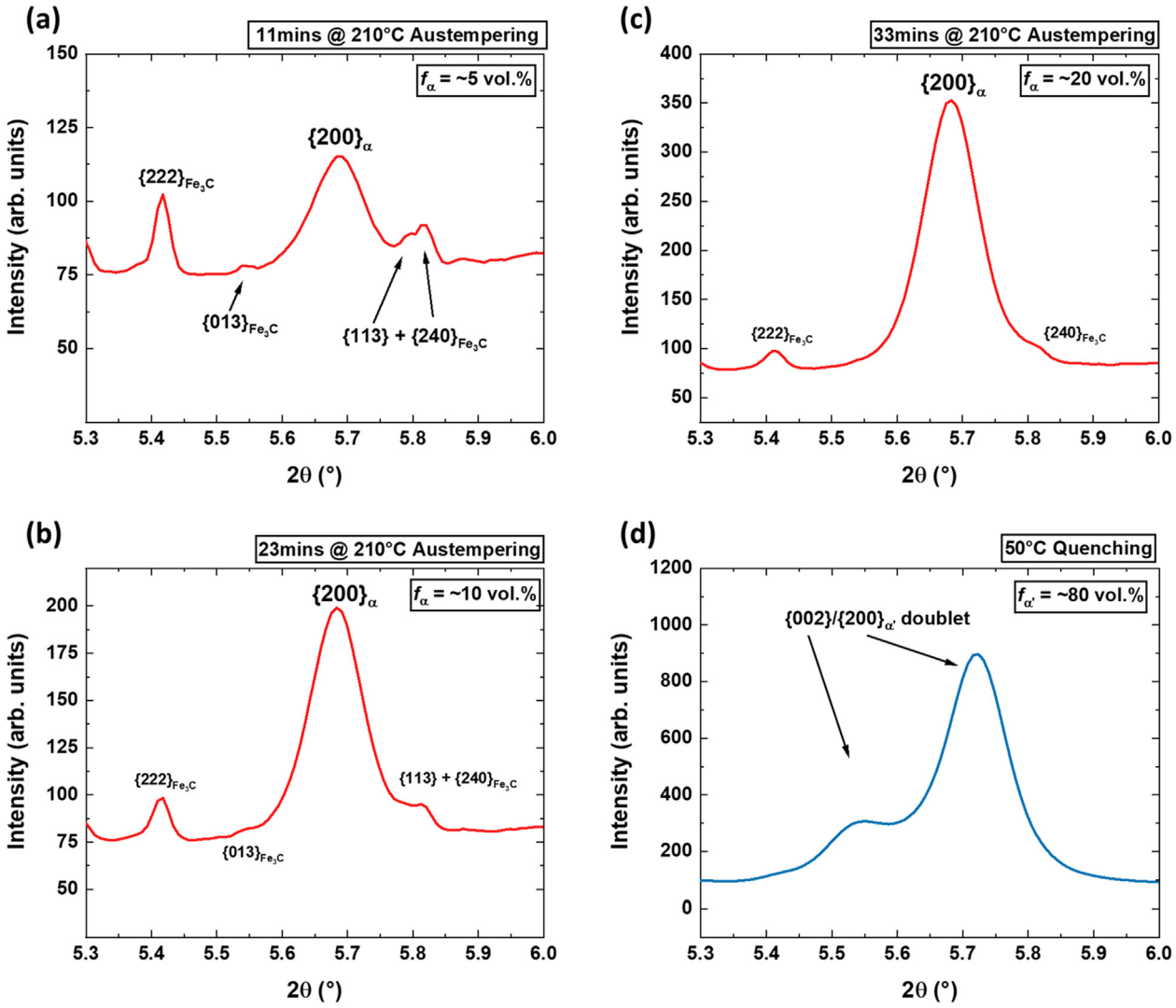

Fig. 3 – Raw 1-D XRD data showing (a) the cubic {200}$_\alpha$ reflection of bainitic ferrite at an austempering temperature of 210 °C. The pattern was measured at t = 11.3 min into the austempering regime. The sample presented a volume fraction of bainitic ferrite of 5.0 ± 0.5 vol.%. (b) & (c) show subsequent plots after 23 min and 33 min of austempering and ~10 vol.% and ~20 vol.% of bainitic ferrite, respectively. (d) Shows a comparable {002}/{200}$_{\alpha'}$ martensite doublet characteristic of tetragonal symmetry, measured at 50 °C after quenching from an austenitisation temperature of 860 °C (adapted from reference [34]). The {222}, {013}, {113} and {200}$_{Fe3C}$ cementite reflections are also labelled in (a).

point that the experimental resolution limit was reached, and the apparent increase in volume fraction beyond this point lies with the experimental error bars. The post-austempering lattice parameter and FWHM of austenite as measured at room temperature are included in Fig. 8b as reference.

Following the additional 120 min of tempering at 340 °C, a reduction in Vickers hardness from 720 $HV_{0.5}$ to 650 $HV_{0.5}$ was also observed from when the sample was austempered at 240 °C (shown in Fig. 9). Compared to the carbide morphologies of bainite formed at 240 °C, after tempering at 340 °C for 1 h, the carbides became more spatially dispersed (Fig. 9a and b). With tempering for 2 h (Fig. 9c), the aspect ratio of the carbides tends to decrease and, compared to tempering for 1 h, a slight change in the shape of the carbides can be noticed, where carbides tend to be spherical. At longer tempering times, the FWHM of the {310}$_\alpha$ reflection continued to decrease and appeared to induce a simultaneous reduction in the sample's length (see Fig. 8c). The {310}$_\alpha$ FWHM exhibited a markedly lower magnitude than the post-austempering room temperature value obtained for sample B240C. During this time, the lattice parameter of the bainitic ferrite remained constant.

4. Discussion

4.1. *Formation and evolution of bainitic ferrite*

Bainitic ferrite starts to form within ~3 min of having reached the target austempering temperature for all samples, but the transformation only completes after 120 min at 270 °C. The final volume fraction of bainitic ferrite measured after the

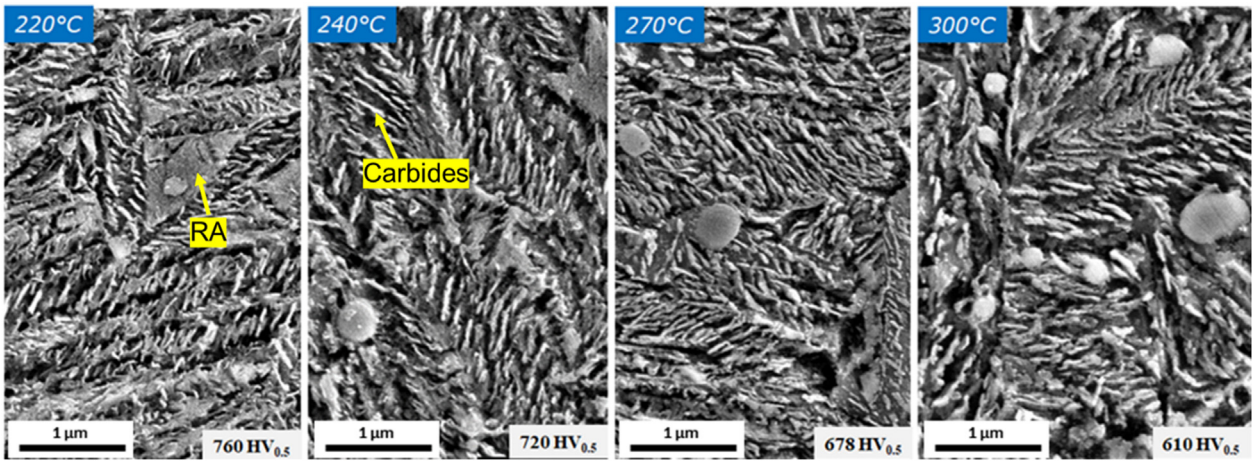

Fig. 4 – Scanning electron micrographs showing the microstructural morphology of SAE 52100 steel after 120 min at austempering temperatures of 220, 240, 270 and 300 °C, with a prior solution annealing at 860 °C for 20 min. The Vickers hardness value using a load of 0.5 kg ($HV_{0.5}$) is given in the bottom right corner of each micrograph. The metallographic samples were etched with 2 vol.% nital solution. The data at 300 °C has been included to compare and better appreciate the changes in aspect ratio of carbides in bainite and in Vickers hardness due to increasing austempering temperature for the same time of 120 min.

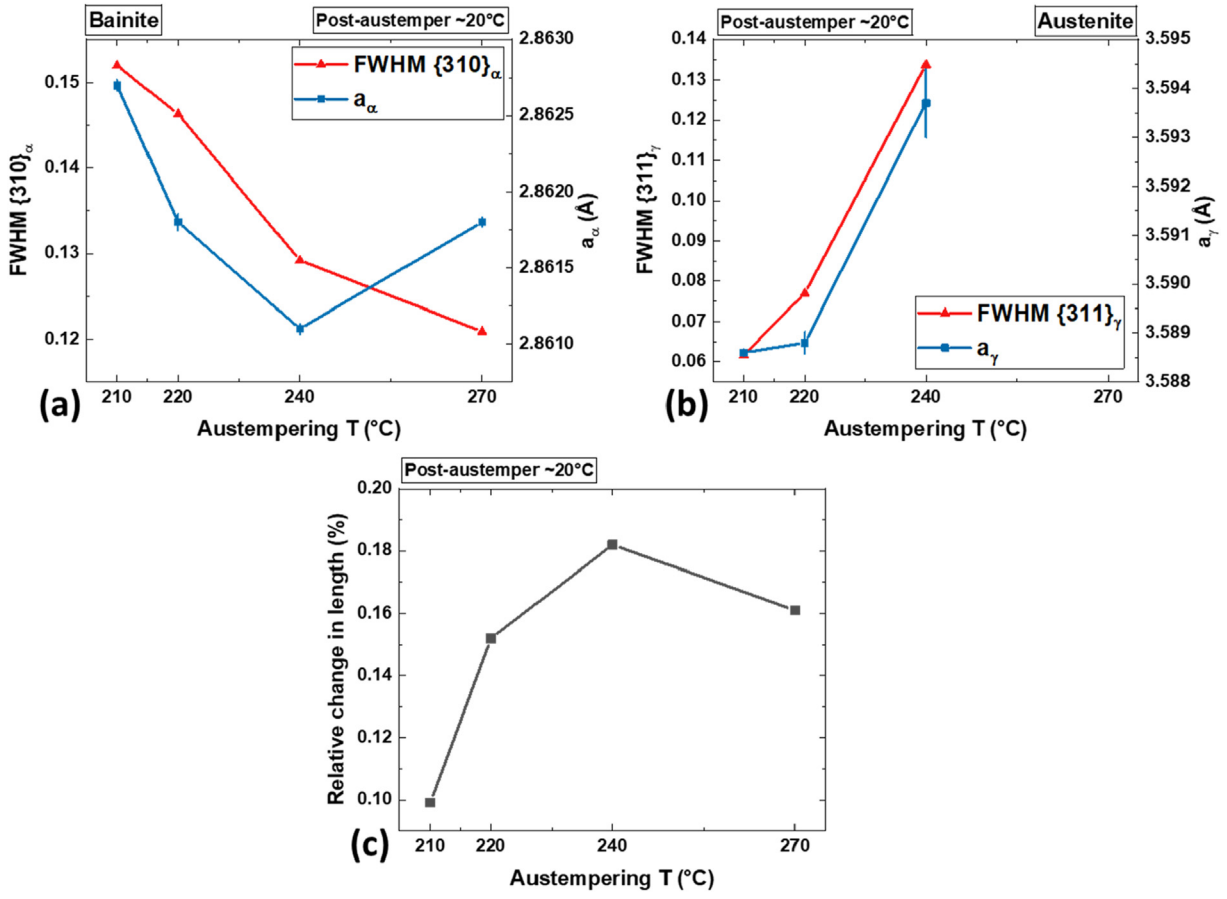

Fig. 5 – (a) The austempering temperature dependence of the lattice parameter of bainitic ferrite, a_α, and FWHM of the $\{310\}_\alpha$ reflection, measured at room temperature post-austempering. (b) The corresponding austempering temperature dependence of the austenite lattice parameter, a_γ, and the FWHM of the $\{311\}_\gamma$ reflection. (c) Relative change in sample length, measured at room temperature after austempering, with respect to the value measured in the initial as-spheroidised condition.

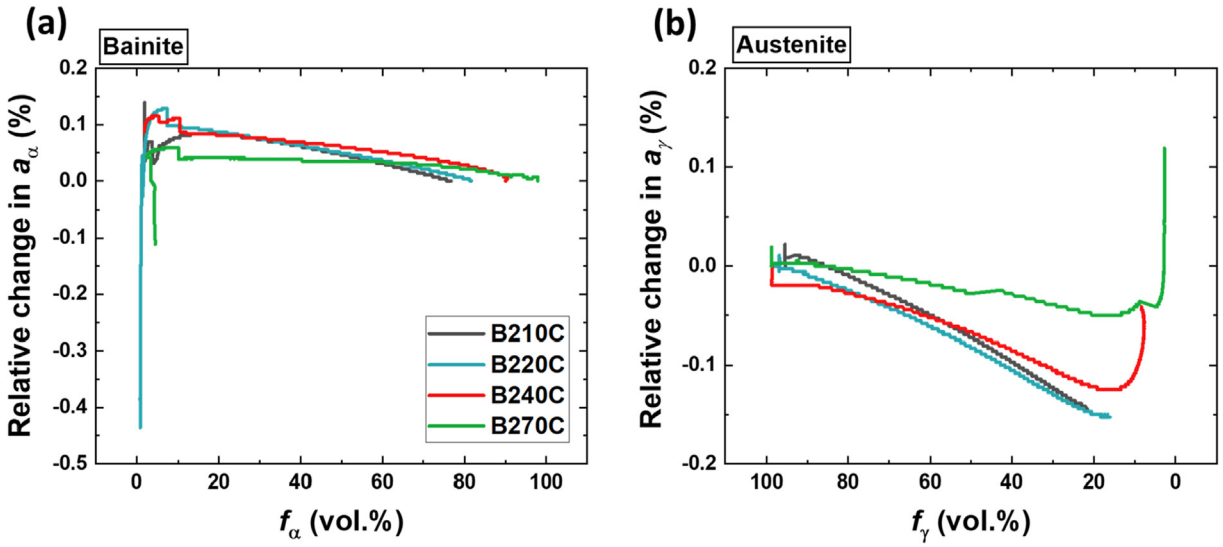

Fig. 6 – Relative change in bainitic ferrite (a) and austenite (b) lattice parameter as a function of volume fraction of bainitic ferrite formed and of remaining austenite, respectively, during austempering for all samples studied. For bainitic ferrite, the change in lattice parameter is relative to the value measured at t = 120 min at the respective austempering temperature; for austenite, it is relative to t = 0 at the respective austempering temperature.

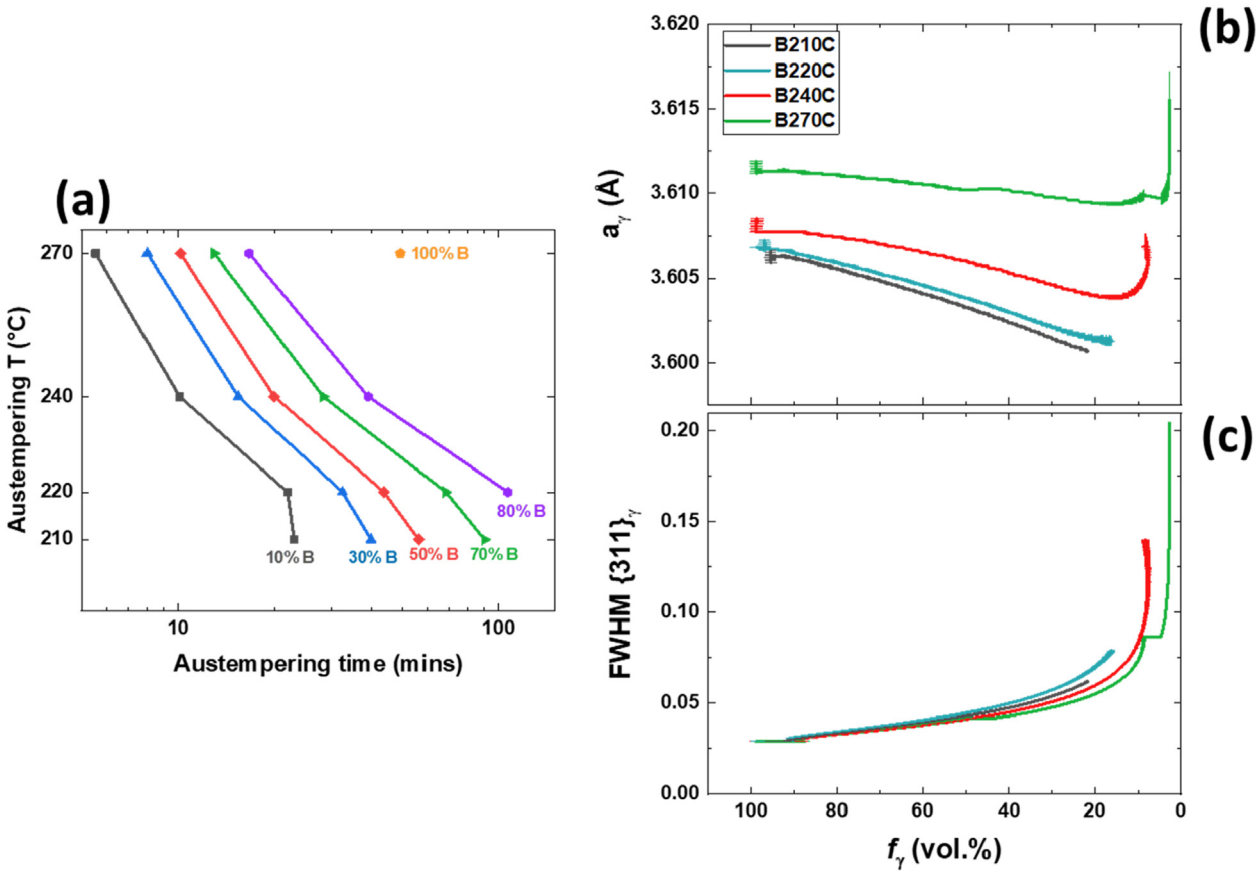

Fig. 7 – (a) The time–temperature-transformation (TTT) diagram as acquired from the synchrotron diffraction data. (b) The austenite lattice parameter, a_γ, as a function of austenite volume fraction, where ~100 vol.% corresponds to the start of austempering, and (c) the corresponding FWHM of the $\{311\}_\gamma$ reflection.

Table 3 – Lattice parameter and FWHM of bainitic ferrite (α) and austenite (γ) for each austempering temperature (T_{aus}), together with the relative change in sample length with respect to the initial as-spheroidised condition, as measured at room temperature after 120 min of austempering.

T_{aus} (°C)	a_α (Å)	FWHM $\{310\}_\alpha$	a_γ (Å)	FWHM $\{311\}_\gamma$	Relative Change in Length (%)
210	2.86270(4)	0.1520	3.58860(8)	0.0671	0.099
220	2.86180(6)	0.1463	3.58880(23)	0.0770	0.152
240	2.86110(4)	0.1292	3.59370(70)	0.1338	0.182
270	2.86180(3)	0.1209	–	–	0.161

heat treatment is also dependent on the austempering temperature, which is attributed to the enhanced transformation kinetics at high temperature. Higher temperatures increase the carbon diffusivity and potential detachment from lattice defects within bainitic ferrite, and it is the carbon ejection from the ferrite lattice and potentially into the remaining austenite ahead of the moving transformation front, that constitutes the limiting step of the process [8]. Carbon can precipitate out as fine carbide particles. In fact, at 270 °C a mixture of lower and upper bainite is generated in high-carbon bearing steel [48].

The initial bainitic ferrite presents a relatively high average lattice parameter as compared to longer austempering times, whereas the $\{310\}_\alpha$ FWHM increases with time after the incubation period and up to a maximum value that depends on temperature. This steel grade is reported to have a bainite start temperature of $B_S = 450$ °C, with a predominance of lower bainite at temperatures lower than ~350 °C [36]. For reference, this steel presents a martensite start temperature of $M_s = 209 \pm 15$ °C at a quench rate of 60 °C/s, as measured under identical experimental conditions as the current presented work [34]. Bundles of adjacent bainitic ferrite laths

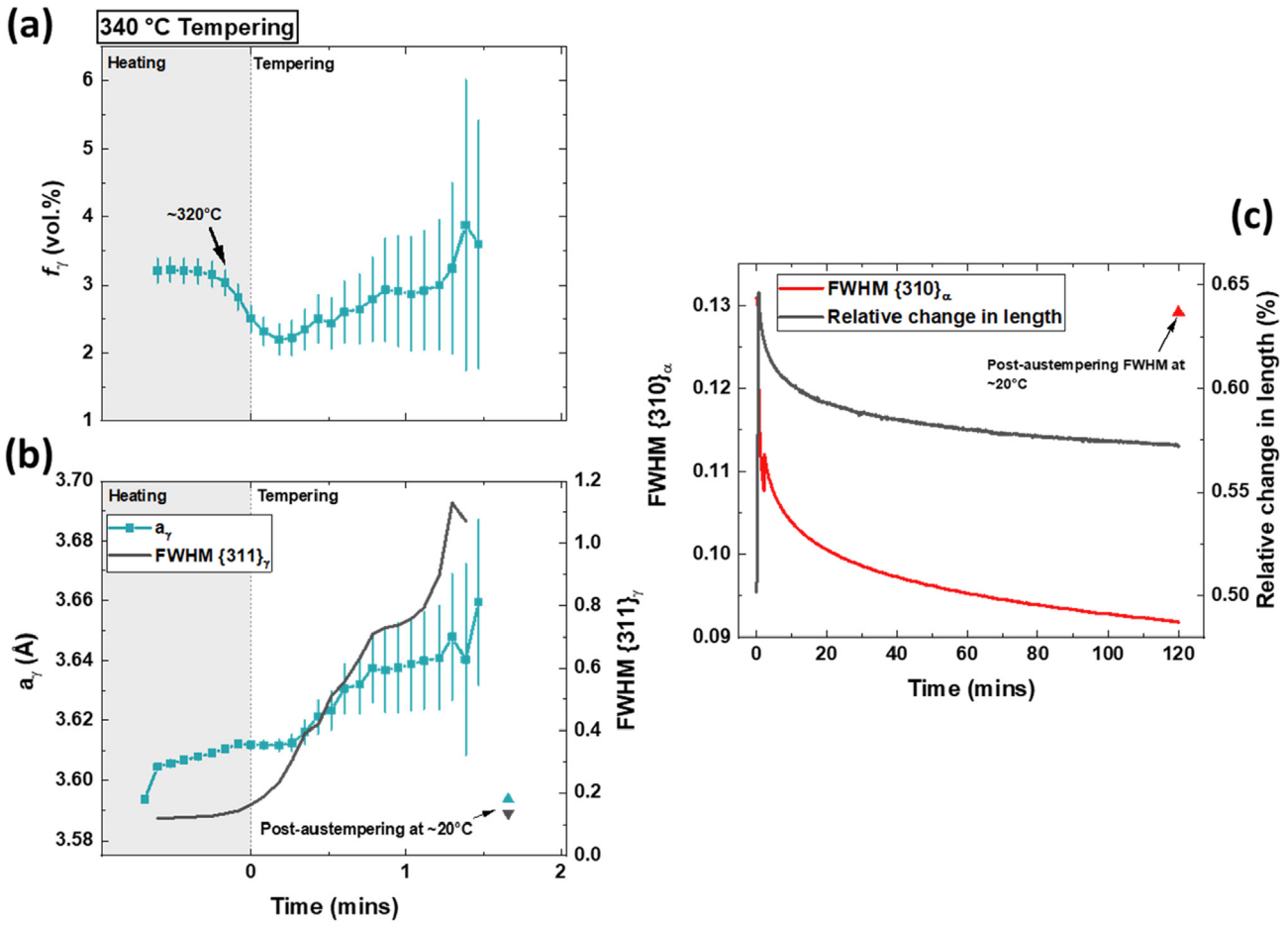

Fig. 8 – (a) Volume fraction of austenite, and (b) the austenite lattice parameter, a_γ, and the FWHM of the $\{311\}_\gamma$ reflection as a function of tempering time at 340 °C. The shaded gray area before t = 0 indicates heating step from the austempering temperature of 240 °C. (c) The relative change in sample length and in FWHM of the $\{310\}_\alpha$ reflection as a function of the tempering time up to 120 min.

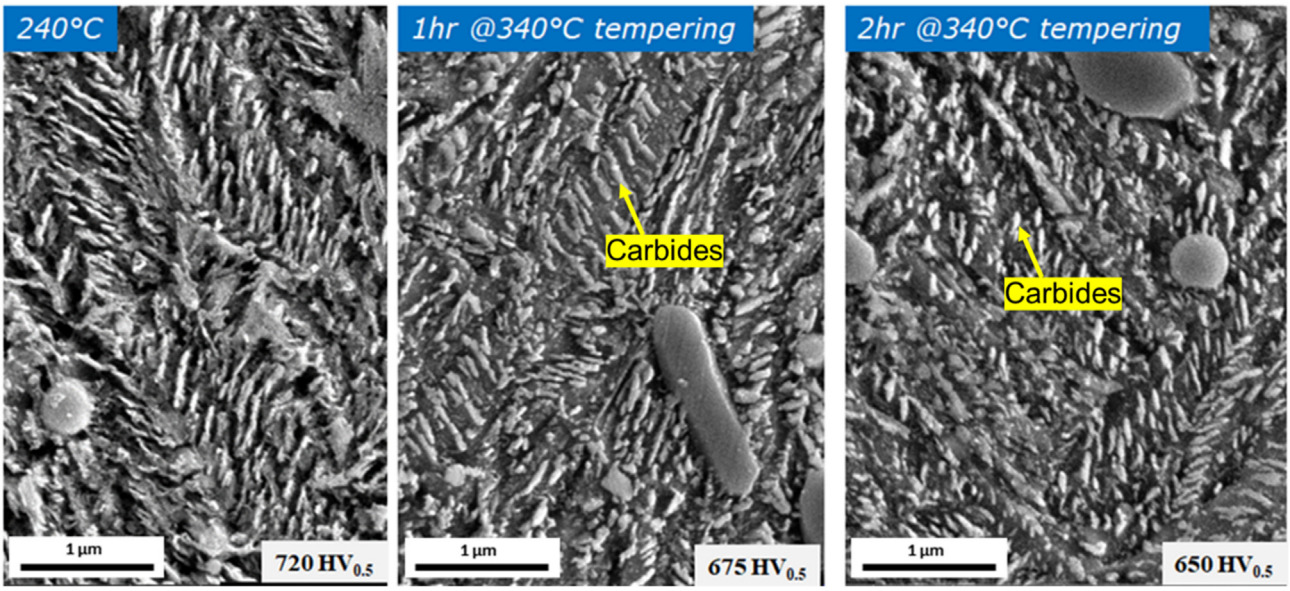

Fig. 9 – Scanning electron micrographs showing the microstructural morphology of SAE 52100 steel in the austempered state at 240 °C for 120 min, and also after a subsequent tempering at 340 °C for either 1 or 2 h. The Vickers hardness value using a load of 0.5 kg ($HV_{0.5}$) is given in the bottom right corner of each micrograph. The metallographic samples were etched with 2 vol.% nital solution.

supersaturated in carbon formed with similar crystallographic orientation, potentially through a shear mechanism [37–39]. Convergent beam electron diffraction measurement of the local lattice parameter in the bainitic ferrite revealed a higher carbon content than anticipated from equilibrium [40]. Moreover, in-situ transmission electron microscopy at elevated temperatures evidenced a significant carbon supersaturation locally that is still present during the growth of bainitic ferrite [41].

The amount of carbon dissolved in the lattice proved to be insufficient to induce a significant tetragonal distortion in the newly forming bainitic ferrite in this steel composition (see Fig. 3a). It remains possible that some tetragonal distortion may have been present during nucleation, but no statistically significant evidence of such a phenomenon was observed within the resolution of this experiment. Certainly, once at least ~5 vol.% bainitic ferrite had formed, the bainitic ferrite had functionally assumed a cubic symmetry and could only be effectively refined with the Rietveld method as such. However, recent work suggests low-temperature bainitic ferrite can present with tetragonal symmetry, albeit at a magnitude three times lower than expected in as-quenched martensite [34,42]. Shown in Fig. 3d is the clear $\{002\}/\{200\}_{\alpha'}$ doublet obtained by quenching the same steel from austenitisation to 50 °C. The c/a ratio of martensite in this instance was ~1.03 [34]. The comparatively low amount of Si (i.e. 0.27 wt.%) in the SAE 52100 steel of this present work may contribute to an enhanced precipitation of carbides as compared with the 2.90 wt.% of Si of the referenced study [42], potentially limiting the degree to which the newly forming bainitic ferrite can be supersaturated with carbon, and hence also limiting the degree of tetragonal distortion that can be achieved.

It was expected that the austenite-to-bainitic ferrite transformation kinetics at these relatively low austempering temperatures of 210 °C–270 °C would be governed by the carbon diffusion within and out of the supersaturated bainitic ferrite [43]. Carbon atoms from supersaturated bainitic ferrite tend to segregate in the vicinity of dislocations, and they lead to the formation of a single carbide variant with plate-like morphology close to the interface as the bainitic ferrite grows [37,44]. The degree of carbon segregation in bainitic ferrite increases at lower temperatures where the dislocation density is higher [45].

There is an equal probability of forming ε-carbide ($Fe_{2.4}C$) and θ-cementite (Fe_3C) in bainitic ferrite from a thermodynamics standpoint, based on density-functional theory calculations, whereas cementite formation is preferential in austenite [46,47]. An η-carbide (Fe_2C) has also been reported in high-silicon high-carbon bainitic steel from X-ray synchrotron diffraction data [42], akin to the tempering of martensite [48], and also other carbon-enriched features from atom probe tomography (APT) data [49]. ε-Carbide tends to preferentially form in regions of lower dislocation density in bainitic ferrite [44], i.e. in the early stages of austempering, and transforms into cementite at longer times in SAE 52100 steel [47], based on TEM and APT data. The predominant carbide in lower bainitic ferrite formed in SAE 52100 steel, as evidenced by TEM data, is cementite [3,50,51]. The presented in-situ XRD results showed that the lattice parameter of the bainitic ferrite was higher at shorter times in all studied samples, and decreased steadily as the transformation proceeded for longer times (see Figs. 2d, 5a and S2b). During the formation of lower bainite, the carbon demand for carbide formation within the ferritic laths competes with the carbon partitioning into the remaining

austenite [52]. A larger loss of carbon into austenite at higher austempering temperatures implies a reduced degree of carbon segregation and a lower driving force for carbide formation within the bainitic ferrite.

Lower bainitic ferrite forms in sheaf-like morphologies and elongated carbides grow within each sheaf and between sheaves [53]. As seen in Fig. 4, the SEM images reveal such nano-sized long carbides that are present within and between bainitic ferrite sheaves. These morphologies are revealed as the surrounding ferritic matrix is etched by the nital solution. In addition, as seen in Fig. 4, as the bainite formation temperature increases (210–270 °C), the carbide morphologies tend to coarsen as the carbon diffusivity and kinetics of bainitic transformation increase with temperature.

The associated transformation strains during the bainitic ferrite growth caused the formation of a high density of crystallographic defects, including dislocations and twins inside the bainitic ferrite laths and in its surrounding untransformed austenite [44,54]. Those strains limited the lath growth and assisted in the nucleation of new plates as an autocatalytic effect [37]. The dislocation density in bainitic ferrite has been reported to increase with decreasing transformation temperature and lath thickness [45,46,55]. The results of this study showed that in higher volume fractions of bainitic ferrite, the FWHM began to reduce gradually, and the minimum volume fraction of bainitic ferrite required to detect this effect increased at lower austempering temperatures (Fig. 2c). This reduction in FWHM suggests that the tempering of the already formed bainitic ferrite had initiated. It also suggests the possibility of the initiation of the recovery of the bainitic ferrite defect structure during austempering, despite the fact that new bainitic ferrite laths were being formed. However, this strain relaxation effect did not significantly influence the change in sample length, which was still dominated by the volume expansion created by the phase transformation (see inset in Fig. 2b).

4.2. *Austenite behaviour during austempering*

The lattice parameter of austenite reduced continuously with time as the transformation from austenite to bainitic ferrite progressed, as seen in Fig. 6b. However, the rate of reduction was lower at higher austempering temperatures, providing evidence of the concomitant carbon partitioning from bainitic ferrite into austenite. There is a competing effect between the expected reduction in lattice parameter and carbon enrichment. The rate of reduction is due to isostatic compressive stresses generated from the volume expansion associated with the FCC to BCC transformation as bainitic ferrite forms from austenite. Carbon enrichment, on the other hand, is expected to increase the austenite lattice parameter. At 240 °C and 270 °C, there was even an increase in the austenite lattice parameter with decreasing volume fraction of austenite when approx. 12–15 vol.% austenite still remains untransformed. It should be further noted that, within the experimental resolution of this work, accurate measurement of the lattice parameter of austenite was only attainable above ~2 vol.%, after which, large relative errors in refinement parameters became apparent. Fig. S3 shows the relative error of the lattice parameter of austenite as a function of its volume fraction. The higher austempering temperatures of 240 and 270 °C, where the recovery of the bainite defect structure occurs at an earlier stage and can consequently favour the possible carbon detachment from pinning sites (e.g. dislocations) and enhanced diffusivity, would promote a higher carbon redistribution towards the remaining 12–15 vol.% austenite. This would cause the observed increase in lattice parameter despite the simultaneous lattice contraction due to the change in volume during in the austenite-to-bainitic phase transformation.

Carbon enrichment in austenite is expected to be inhomogeneous and to be higher in the immediate vicinity of the bainitic ferrite laths or in regions trapped between the laths [56]. Also, a higher density of dislocations close to the bainitic ferrite–austenite interface is expected [44]. An enhanced local carbon enrichment in the remaining austenite at 270 °C, esp. Close to that interface, can lead to a further enhancement of the austenite-to-bainitic ferrite transformation kinetics. Additional carbon atoms in solid solution in austenite result in higher chemical stability [57], and consequently to a lower tendency of austenite to transform into bainitic ferrite. However, the local carbon enrichment also increases the driving force for carbide precipitation, potentially exceeding the solubility limit of carbon in austenite [44]. The consequence of carbon loss in the form of carbides is a reduction in carbon content and stability in austenite that would further transform into bainitic ferrite [44,58]. It was at the temperature of 270 °C that the austenite transformation was complete within ~50 min. In addition, it is noteworthy that a mixture of lower and higher bainite has been reported in 1.2 wt.%C steel in the temperature region of 250°–375 °C [43].

4.3. *Austempered microstructures at room temperature*

The measured lattice parameter of bainitic ferrite austempered at 270 °C was higher than that at 240 °C, whereas the FWHM continued its inversely proportional relationship with austempering temperature up to 270 °C (Fig. 5a). These observations suggest that an abnormally high carbon content is retained in the lattice of bainitic ferrite after 120 min of austempering at that temperature. There is a continuous competition for carbon to either precipitate as fine carbides within the bainitic ferrite or partition into untransformed austenite grains. It is only at this highest temperature of 270 °C that a full austenite-to-bainitic ferrite transformation was observed during austempering. Therefore, even though carbon significantly partitions into austenite at that temperature, the last higher-carbon austenite grains transformed into bainitic ferrite after only 50 min within the experimental resolution, and those final transforming austenite grains can generate on average higher carbon bainitic ferrite laths.

Additionally, at 270 °C, the recovery of the local lattice strains (e.g., from dislocations and other lattice defects generated during the transformation itself) starts at an earlier stage during austempering, as evidenced by the reduction in FWHM of the $\{310\}_{\alpha}$ reflection (Fig. 2c and a). This can cause a reduction of potential nucleation sites for carbon clustering and formation of nano-sized carbide particles within the

bainitic ferrite. Consequently, the higher transformation rate to completion at 270 °C and the earlier recovery of the lattice strains could be the cause of the lattice parameter of the bainitic ferrite detected at room temperature in the B270C sample being higher than that of the B240C sample.

The room temperature value of FWHM of the $\{310\}_{\alpha}$ reflection decreased for higher austempering temperatures (Fig. 5a). In contrast, the progression of the austenite-to-bainitic ferrite transformation caused an increase in both the FWHM of the $\{311\}_{\gamma}$ reflection and of the austenite lattice parameter from 210 °C to 240 °C, due to a higher accumulation of dislocations and carbon in the remaining austenite. Moreover, the relative change in sample length measured at room temperature increased with the increase of austempering temperature from 210 °C to 240 °C. At the highest temperature of 270 °C, that length change decreased relative to its value at 240 °C. It was at 270 °C that the austenite transformation reached completion within the 120 min of austempering in this experiment, together with the earlier start of the tempering of the already formed bainitic ferrite and the associated recovery of the lattice defects such as dislocations during austempering.

As a comparison, an equivalent sample that was quenched from 860 °C down to 50 °C produced ~79 vol.% of tetragonal martensite (α') (see Fig. 3b). During isothermal holding for 20 min at 50 °C before the final cooling step to room temperature, the sample experienced a reduction in the $c_{\alpha'}/a_{\alpha'}$ ratio and only an additional ~2 vol.% martensite was detected [34]. At room temperature, the value of the FWHM of the $\{310\}_{\alpha'}$ reflection was 0.1481°, lower than the equivalent value for the austempered samples in this study, whereas the relative change in sample length amounted to 0.2431%. These results confirm the higher degree of relaxation of the lattice distortion in tetragonal martensitic steel compared to the austempered microstructures, and consequently a larger impact on the dimensional stability of the material.

4.4. *Strain relaxation during tempering*

The recovery of the ferrite lattice strains that was initiated during the austempering at 240 °C continued during the subsequent tempering at 340 °C, as revealed by the steady reduction in FWHM of the $\{310\}_{\alpha}$ reflection (Fig. 8c). In addition, raising the temperature to 340 °C leads to increased carbon diffusion distances and can promote carbon redistribution further. This result suggests that the recovery of the dislocation structure and other lattice defects is a dominant phenomenon, with possible carbon detachment from pinning sites in the lattice such as dislocations and carbon redistribution, and the potential formation or coarsening of carbide particles. Consequently, there was also a simultaneous reduction in sample length during the 120 min of tempering at 340 °C, despite the lack of further austenite-to-ferrite transformation. At 340 °C tempering, significant partitioning of substitutional solutes is not expected [59]. In addition, the reduction of material hardness with tempering (Fig. 9) matches the lattice strain relaxation evidenced by the lowered FWHM of the $\{310\}_{\alpha}$ values. In fact, as shown in Fig. 8a-c, with tempering treatment at 340 °C, the carbon redistribution promotes the morphological changes in the carbides. Typically, and as suggested in literature [60], at temperatures above 300 °C, the ε-carbides tend to dissolve and rod shaped cementite particles precipitate and coarsen with the tempering time. As seen in Fig. 9b and c, as tempering time increases, the rod shaped carbide particles tend to coarsen and spheroidise (decreased aspect ratios), possibly to minimise their interfacial energy with the surrounding matrix.

5. Conclusions

In this study, we monitored the formation of bainitic ferrite and the microstructural evolution therein of SAE 52100 steel in the range of austempering temperatures of 210 °C–270 °C via in-situ high-energy X-ray diffraction and dilatometry. The austenite-to-bainitic ferrite transformation brought about significant lattice strains in both the parent austenite and the newly formed ferritic laths, as evidenced by the steady increase in FWHM of the $\{311\}_{\gamma}$ and $\{310\}_{\alpha}$ reflections, respectively. The bainitic ferrite presented a relatively high value of lattice parameter in the early stages of austempering. However, there was a significant reduction in the ferrite lattice parameter at longer times, ascribed to the carbon segregation close to dislocations and other lattice defects and the subsequent nano-scaled carbide precipitation.

At the temperatures of 240 °C and 270 °C, the increase in the austenite lattice parameter at longer austempering times flagged the simultaneous carbon partitioning into the remaining austenite. The recovery of the defect structure and local lattice strains associated with the tempering of the already formed bainitic ferrite had begun occurring at the austempering temperature, but was enhanced during the subsequent tempering at 340 °C. The change in sample length during austempering was dominated by the volume change during the phase transformation up to its completion, whereas during tempering, it was the recovery of lattice defects in the bainitic ferrite that primarily affected the dimensional stability of the material.

Declaration of Competing Interest

The authors declare that they have no known competing financial interests or personal relationships that could have appeared to influence the work reported in this paper.

Acknowledgments

This work was made possible by financial support and samples provided by The Timken Company. We also acknowledge the PETRA-III synchrotron facility at DESY (Germany) for the time we were granted on the P07 beam line under proposal I-20180929 EC. The authors declare that they have no known competing financial interests or personal relationships that could have appeared to influence the work reported in this paper.

Appendix A. Supplementary data

Supplementary data to this article can be found online at https://doi.org/10.1016/j.jmrt.2022.05.025.

REFERENCES

[1] Harris TA. Rolling bearing analysis. 4th ed. John Wiley & Sons; 2001.
[2] Zaretsky EV. Rolling bearing steels – a technical and historical perspective. Mater Sci Technol 2012;28:58–69.
[3] Bhadeshia HKDH. Steels for bearings. Prog Mater Sci 2012;57:268–435.
[4] Paladugu M, Hyde RS. Influence of material, heat treatment, and microstructure in resisting white etching crack damage. In: Beswick J, editor. Bearing steel technologies: 12th volume, progress in bearing steel metallurgical testing and quality assurance. West Conshohocken, PA: ASTM International; 2020. p. 182–201. https://doi.org/10.1520/STP162320190039.
[5] Paladugu M. In: Beswick J, editor. Lubricant-induced white etching cracks: Mechanism and Effects of surface finishing in bearing steel technologies: 12th volume, progress in bearing steel metallurgical testing and quality assurance. West Conshohocken, PA: ASTM International; 2020. p. 131–46. https://doi.org/10.1520/STP162320190112.
[6] Paladugu M, Lucas DR, Scott Hyde R. Influence of raceway surface finish on white etching crack generation in WEC critical oil under rolling-sliding conditions. Wear 2019;422:81–93.
[7] Rocha Ada S, Hirsch T. Fast in situ X-ray diffraction phase and stress analysis during complete heat treatment cycles of steel. Mater Sci Eng 2005;395:195–207.
[8] Jimenez-Melero E, Blondé R, Sherif MY, Honkimäki V, van Dijk NH. Time-dependent synchrotron X-ray diffraction on the austenite decomposition kinetics in SAE 52100 bearing steel at elevated temperatures under tensile stress. Acta Mater 2013;61:1154–66.
[9] Voskamp AP, Österlund R, Becker PC, Vingsbo O. Gradual changes in residual stress and microstructure during contact fatigue in ball bearings. Met. Technol. 1980;7:14.
[10] Dommarco RC, Kozaczek KJ, Bastias PC PC, Hahn GT, Rubin CA. Residual stresses and retained austenite evolution in SAE 52100 steel under non-ideal rolling contact loading. Wear 2004;257:1081–8.
[11] Vegter RH, Verschoor HA, Girones A. X-ray microdiffraction for the analysis of bearing operation conditions. ASTM Int 2006;3(7):JAI14058.
[12] Gegner J. Tribological aspects of rolling bearing failures. In: Kuo CH, editor. Tribology. Lubricants and lubrication. IntechOpen; 2011.
[13] Paladugu M, Hyde RS. Influence of microstructure on retained austenite and residual stress changes under rolling contact fatigue in mixed lubrication conditions. Wear 2018;406–407:84.
[14] Voskamp A. Microstructural changes during rolling contact fatigue. PhD thesis. The Netherlands: Delft University of Technology; 1997.
[15] Oezel M, Janitzky T, Beiss P, Broeckmann C. Influence of steel cleanliness and heat treatment conditions on rolling contact fatigue of 100Cr6. Wear 2019;430–431:272–9.
[16] Chakraborty J, Bhattacharjee D, Manna I. Austempering of bearing steel for improved mechanical properties. Scripta Mater 2008;59:247–50.
[17] Zhang P, Zhang FC, Yan ZG, Wang TS, Qian LH. Wear property of low-temperature bainite in the surface layer of a carburized low carbon steel. Wear 2011;271:697–704.
[18] Zhang F, Yang Z. Development of and perspective on high-performance nanostructured bainitic bearing steel. Engineer 2019;5:319–28.
[19] Liu H, Sun J, Jiang T, Guo S, Liu Y. Improved rolling contact fatigue life for an ultrahigh-carbon steel with nanobainitic microstructure. Scripta Mater 2014;90–91:17–20.
[20] Efremenko VG, Hesse O, Friedrich Th, Kunert M, Brykov MN, Shimizud K, et al. Two-body abrasion resistance of high-carbon high-silicon steel: metastable austenite vs nanostructured bainite. Wear 2019;418–419:24–35.
[21] Stickels CA. Carbide refining heat treatment for 52100 bearing steels. Metall Trans A 1974;5:865–74.
[22] Vetters H, Dong J, Zoch H-W. Effect of residual austenite on properties of tool steel following shortened treatments in lower bainitic phase. Int Heat Treat Surf Eng 2009;3:131–5.
[23] Akbasoglu FC, Edmonds DV. Rolling contact fatigue and fatigue crack propagation in 1C–1.5Cr bearing steel in bainitic condition. Metall Trans A 1990;21:889–93.
[24] Wang Y, Lei TC, Gao CQ. Influence of isothermal hardening on the sliding wear behaviour of 52100 bearing steel. Tribol Int 1990;23:47–53.
[25] Krauss G. Principles of heat treatment of steel. Ohio (US): American Society for Metals; 1980.
[26] Mikus EB, Hughel TJ, Gerty JM, Knusden AC. The dimensional stability of a precision ball bearing material. Trans. ASM 1960;52:307–20.
[27] Foster D, Paladugu M, Hughes J, Kapousidou M, Barcellini C, Daisenberger D, et al. Comparative micromechanics assessment of high-carbon martensite/bainite bearing steel microstructures using in-situ synchrotron X-ray diffraction. Mater 2020;14:100948.
[28] Staron P, Fischer T, Lippmann T, Stark A, Daneshpour S, Schnubel D, et al. In situ experiments with synchrotron high-energy X-rays and neutrons. Adv Eng Mater 2011;13:658–63.
[29] Schell N. Synchrotron-based capabilities for studying engineering materials at PETRA-III. Synch Rad News 2017;30:29–34.
[30] Schell N, King A, Beckmann F, Ruhnau H-U, Kirchhoff R, Kiehn R, et al. The high energy materials science beamline (HEMS) at PETRA III. AIP Conf Proc 2010;1234:391.
[31] Filik J, Ashton AW, Chang PCY, Chater PA, Day SJ, Drakopoulos M, et al. Processing two-dimensional X-ray diffraction and small-angle scattering data in DAWN 2. J Appl Cryst 2017;50:959–66.
[32] Young RA. The Rietveld method. IUCr monographs on crystallography. Oxford University Press; 1993.
[33] Rodríguez-Carvajal J. Recent advances in magnetic structure determination by neutron powder diffraction. Phys. B 1993;192:55.
[34] Foster D, Paladugu M, Hughes J, Kapousidou M, Islam U, Stark A, et al. In-situ synchrotron X-ray diffraction during quenching and tempering of SAE 52100 steel. Mater Today Commun 2021;29:102930.
[35] Masoumi M, Echeverri EAA, Tschiptschin A, Goldenstein H. Improvement of wear resistance in a pearlitic rail steel via quenching and partitioning processing. Sci Rep 2019;9:7454.
[36] Hollox GE, Hobbs RA, Hampshire JM. Lower bainite bearings for adverse environments. Wear 1981;68:229–40.
[37] Durand-Charre M. Microstructure of steels and cast irons. Springer; 2004.
[38] Shackleton DN, Kelly PM. Morphology of bainite. In: Physical properties of martensite and bainite, special report 93. London: Iron and Steel Institute; 1965. p. 126–34.

[39] Abbaschian R, Abbaschian L, Reed-Hill RE. Physical metallurgy principles. 4th ed. Stamford (USA): Cengage Learning; 2009.
[40] Zhang M-X, Kelly PM. Determination of carbon content in bainitic ferrite and carbon distribution in austenite by using CBKLDP. Mater Char 1998;40:159–68.
[41] Kang MK, Sun JL, Yang QM. High temperature TEM in situ study of lower bainite carbide precipitation. Metall Trans A 1990;21:853–8.
[42] Rementeria R, Jimenez JA, Allain SYP, Geandier G, Poplaswsky JD, Urones-Garrote E, et al. Quantitative assessment of carbon allocation anomalies in low temperature bainite. Acta Mater 2017;133:333–45.
[43] Sajjadi SA, Zebarjad SM. Isothermal transformation of austenite to bainite in high carbon steels. J Mater Process Technol 2007;189:107–13.
[44] H Bhadeshia HKD. Bainite in steels. 3rd ed. IOM Communications Ltd; 2015.
[45] Pickering FB. The structure and properties of bainite in steels. In: Transformation and hardenability in steels. Ann Arbor, Michigan, USA: Climax Molybdenum; 1967. p. 109–32.
[46] Fondekar MK, Rao AM, Mallik AK. Strain tempering of bainite. Metall Trans A 1970;1:885–90.
[47] Song W, von Appen J, Choi P, Dronskowski R, Raabe D, Bleck W. Atomic-scale investigation of ε and θ precipitates in bainite in 100Cr6 bearing steel by atom probe tomography and ab initio calculations. Acta Mater 2013;61:7582–90.
[48] Han K, van genderen MJ, Böttger A, Zandbergen HW, Mittemeijer EJ. Initial stages of Fe-C martensite decomposition. Phil Mag A 2001;81(3):741–57.
[49] De-Castro D, Rementeria R, Vivas J, Sourmail T, Poplawsky JD, Urones-Garrote E, et al. Examining the multi-scale complexity and the crystallographic hierarchy of isothermally treated bainitic and martensitic structures. Mater Char 2020;160:110127.
[50] Swahn H, Becker PC, Vingsbo O. Electron-microscope studies of carbide decay during contact fatigue in ball bearings. Met Sci 1976;10(1):35–9.
[51] Vetters H, Dong J, Bornas H, Hoffman F, Zoch H-W. Microstructure and fatigue strength of the roller-bearing steel 100Cr6 (SAE 52100) after two-step bainitisation and combined bainitic–martensitic heat treatment. Int J Mater Res 2006;97:1432–40.
[52] Bhadeshia HKDH. The lower bainite transformation and the significance of carbide precipitation. Acta Metall 1980;28:1103–14.
[53] D Fielding LC. The bainite controversy. Mater Sci Technol 2013;29(4):383–99.
[54] Chang LC, Bhadeshia HKDH. Metallographic observations of bainite transformation mechanism. Mater Sci Technol 1995;11(2):105–8. 1995.
[55] He SH, He BB, Zhu KY, Huang MX. On the correlation among dislocation density, lath thickness and yield stress of bainite. Acta Mater 2017;135:382–9.
[56] Garcia-Mateo C, Caballero FG, Miller MK, Jimenez JA. On measurement of carbon content in retained austenite in a nanostructured bainitic steel. J Mater Sci 2012;47:1004–10.
[57] Jimenez-Melero E, van Dijk NH, Zhao L, Sietsma J, Offerman SE, Wright JP, et al. Martensitic transformation of individual grains in low-alloyed TRIP steels. Scripta Mater 2007;56(5):421–4.
[58] Spanos G, Fang HS, Aaronson HI. A mechanism for the formation of lower bainite. Metall Trans A 1990;21:1381–90.
[59] Peet MJ, Babu SS, Miller MK, Bhadeshia HKDH. Tempering of low-temperature bainite. Metall Mater Trans A 2017;48A:3410–8.
[60] Yamasaki S. Modelling precipitation of carbides in martensitic steels. Doctoral Thesis. University of Cambridge; 2004.